POLITECNICO DI TORINO
Repository ISTITUZIONALE

Thermal-hydraulic analysis of the DTT CS and PF pulsed coil performance during AC operation

(Article begins on next page)

19 May 2024

Thermal-hydraulic analysis of the DTT CS and PF pulsed coils performance during AC operation

R. Bonifetto[a], A. Di Zenobio[b], L. Muzzi[b], S. Turtù[b], R. Zanino[a], A. Zappatore[a]

[a]*NEMO group, Dipartimento Energia, Politecnico di Torino, Torino, Italy*
[b]*ENEA, Frascati, Italy*

Corresponding author: roberto.bonifetto@polito.it

Abstract

The EU DEMO fusion reactor, now entering in its conceptual design phase, will have to tackle several challenges, such as the long plasma pulse duration and the exhaust of very high heat fluxes from the plasma. The Divertor Tokamak Test (DTT) facility, a compact superconducting tokamak under construction at ENEA Frascati, will address the power exhaust problem in DEMO by testing several DEMO-relevant divertor solutions and operation scenarios.

The DTT superconducting coils are the subject of the analyses presented here: as the tokamak must be very flexible to face different plasma scenarios, the design of the magnet system must be proven to be robust. In particular, the thermal-hydraulic performance of the coils operated in pulsed mode, namely the Central Solenoid (CS) and the Poloidal Field (PF) coils, will be analyzed. The CS is composed of 6 modules, layer-wound with Nb3Sn Cable-in-Conduit Conductors (CICCs), while the PF coils are pancake-wound. The two PF coils closest to the machine axis are wound using Nb3Sn CICCs, while the others adopt NbTi CICCs. All the coils are cooled by supercritical He (SHe) in forced flow.

The pulsed operation of these coils induces AC losses, eroding their temperature margin: a detailed thermal-hydraulic model of the DTT pulsed coils is developed here using the 4C code. The model is then applied to the simulation of the two reference plasma scenarios, a single null and a double null, computing the minimum temperature margin. Different cooling options (single- or double-pancake) are investigated for the PF coils, while the sensitivity to the coupling time constant value is assessed for the CS.

Abbreviations

4C code	Cryogenic Circuit, Conductor and Coil code
AC	Alternated Current
CICC	Cable-in-Conduit Conductor
CS	Central Solenoid
D	Diameter
DN	Double Null
DP	Double Pancake
DPc	Double Pancake cooling
DTT	Divertor Tokamak Test
EoF	End of Flat top

EU DEMO	EUropean DEMOnstrator
HF	High Field
HS	Hot-Spot
ID	Inner Diameter
ITIP	Inter-Turn and Inter-Pancake
LF	Low Field
MF	Medium Field
OD	Outer Diameter
PF	Poloidal Field
SC	SuperConducting
SHe	Supercritical He
SN	Single Null
SoF	Start of Flat top
SP	Single Pancake
SPc	Single Pancake cooling
TF	Toroidal Field
WP	Winding Pack

1   Introduction

The ongoing design of the EUropean DEMOnstrator (EU DEMO) reactor [1] must tackle several challenges, among which the long plasma pulse duration and the large thermal loads [2]. The power exhaust problem asks then for a new, robust design of the divertor. This motivates the design of a satellite fusion experiment, the Divertor Tokamak Test (DTT) facility [3]. It will be a fully superconductive compact tokamak, very flexible in terms of plasma configurations, and will test several DEMO-relevant divertor solutions.

The DTT construction is starting in Frascati, Italy and its magnet system is in the final design stage. The machine will feature a plasma major radius $R_0 \sim 2.19$ m and will reach a toroidal field on the plasma axis of ~ 6 T, with a plasma current of 5.5 MA [4], [5].

The focus is here on the set of superconducting coils operated in pulsed mode, namely the Central Solenoid (CS) and the 6 Poloidal Field (PF) coils, see Fig. 1. The former is composed by 6 modules, layer-wound with Nb3Sn Cable-in-Conduit Conductors (CICCs). The latter are instead pancake-wound, but while the two PF coils closest to the machine axis adopt Nb3Sn strands to withstand magnetic fields as high as ~9 T, the others, subject to magnetic fields well below 6 T, are wound using NbTi CICCs. All the coils are cooled by supercritical He (SHe) in forced flow.

The pulsed operation of these coils causes heat deposition in the strands and jacket due to AC losses. The latter erode the temperature margin during operation, so that besides accurate mechanical design also the thermal-hydraulic performance must be assessed.

A detailed thermal-hydraulic model of the DTT pulsed coils is developed here using the 4C code. The model is applied to the simulation of the two reference plasma scenarios, computing the minimum temperature margin. In the case of the PF coils, different cooling options (single- or double-pancake) are investigated, together with the effect of the thermal coupling among turns and pancakes, while different coupling time constant values are adopted and compared for the calculation of AC losses in the CS.
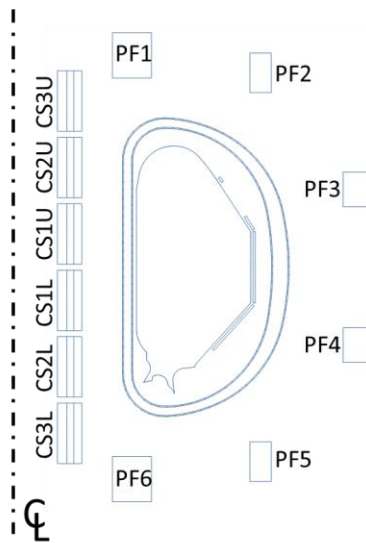

Fig. 1. Radial-vertical cross section of the PF coils and CS. The conventional numbering of the coils and modules is also reported.

2   The DTT pulsed coils

As opposed to the Toroidal Field (TF) coils, whose performance in normal operation at constant current have been analysed in [6], the PF coils and the CS are operated with variable current to induce the current inside the plasma (the CS) and to shape it (the PF). Several different plasma scenarios are being investigated for this flexible machine, but the two reference ones are the Single Null (SN) and the Double Null (DN) scenario, see Fig. 2. After an initial magnetization of the pulsed coils (the "premagnetization"), the plasma current is ramped up by the current variation in the in CS (see Fig. 3), acting as the primary winding of a transformer. At 27 s, the "Start of Flat top" (SoF), the plasma reaches its nominal current

value (5.5 MA and 5 MA in the SN and DN, respectively), kept constant by a (slower) variation of the pulsed coil current variation until the "End of Flat top" (EoF). The duration of the plasma flat top is ~20 s longer in the DN scenario. After the EoF, the plasma is terminated and the pulsed coils are slowly discharged in 60 s. At present, the detailed current evolution during the breakdown (the first instants immediately after the premagnetization, usually experiencing steep variations for a very short time) is being defined, so its effect will be further investigated in the future.

The magnetic field variations (in turn due to the current variations) induce AC losses in the conductors, thus experiencing a temperature increase and consequent temperature margin erosion during their pulsed operation. Therefore, after the CS and PF shutdown following a plasma, during the dwell period (lasting more than 3300 s) the recooling of the coils takes place, until the subsequent plasma pulse, starting 1 hour after the previous one.

In Fig. 3 it is possible to appreciate the different current evolution in the PF coils and in the CS modules during the SN (Fig. 3a and Fig. 3b, respectively) and the DN (Fig. 3c and Fig. 3d, respectively) scenarios. Note that the latter is a completely symmetric scenario from the point of view of the pulsed magnet operation; this symmetry is possible also thanks to the vertical symmetry of the magnet system, see below. Due to the different duration and steepness of the current variations, it is not possible to immediately identify whether the SN or the DN will be the worst scenario from the coil performance point of view, so both of them are analysed in this work.

Both the PF coils and CS magnet systems are cooled by the same SHe circuit: the 6 PF coils are connected in parallel in a (first) branch, while the 6 CS modules are connected in parallel in a second branch. These two main branches are then connected in an outer hydraulic parallel between the two systems. The SHe enters the coils at 4.5 K and ~6 bar, while the cold circulator will be designed to provide a pressure head of ~1 bar across each coil, in nominal operating conditions.
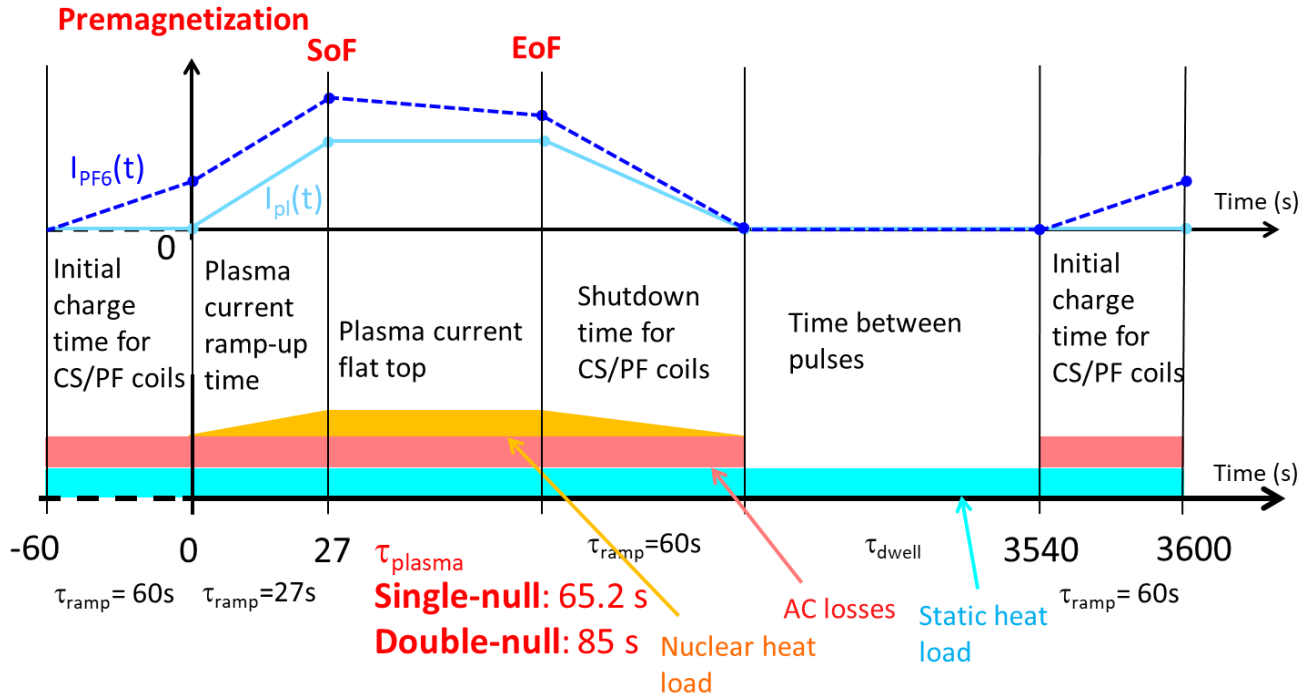
Fig. 2. Plasma pulse evolution in DTT: the (qualitative) evolution of the PF6 current I_{PF6} (dashed line) and plasma current I_{pl} (solid line) is reported in the top part, while the time intervals during which the heat deposition from AC losses, nuclear and static heat load takes place in the magnets are highlighted in light red, yellow and cyan, respectively, at the bottom (the height of the band is not related to the value of the respective heat load). Note that in the convention adopted here, each plasma cycle starts at the premagnetization: to highlight the repetitive pulsed operation, the initial PF and CS current charge at the end of the previous cycle is also reported, before the beginning of the cycle represented here, for negative times.
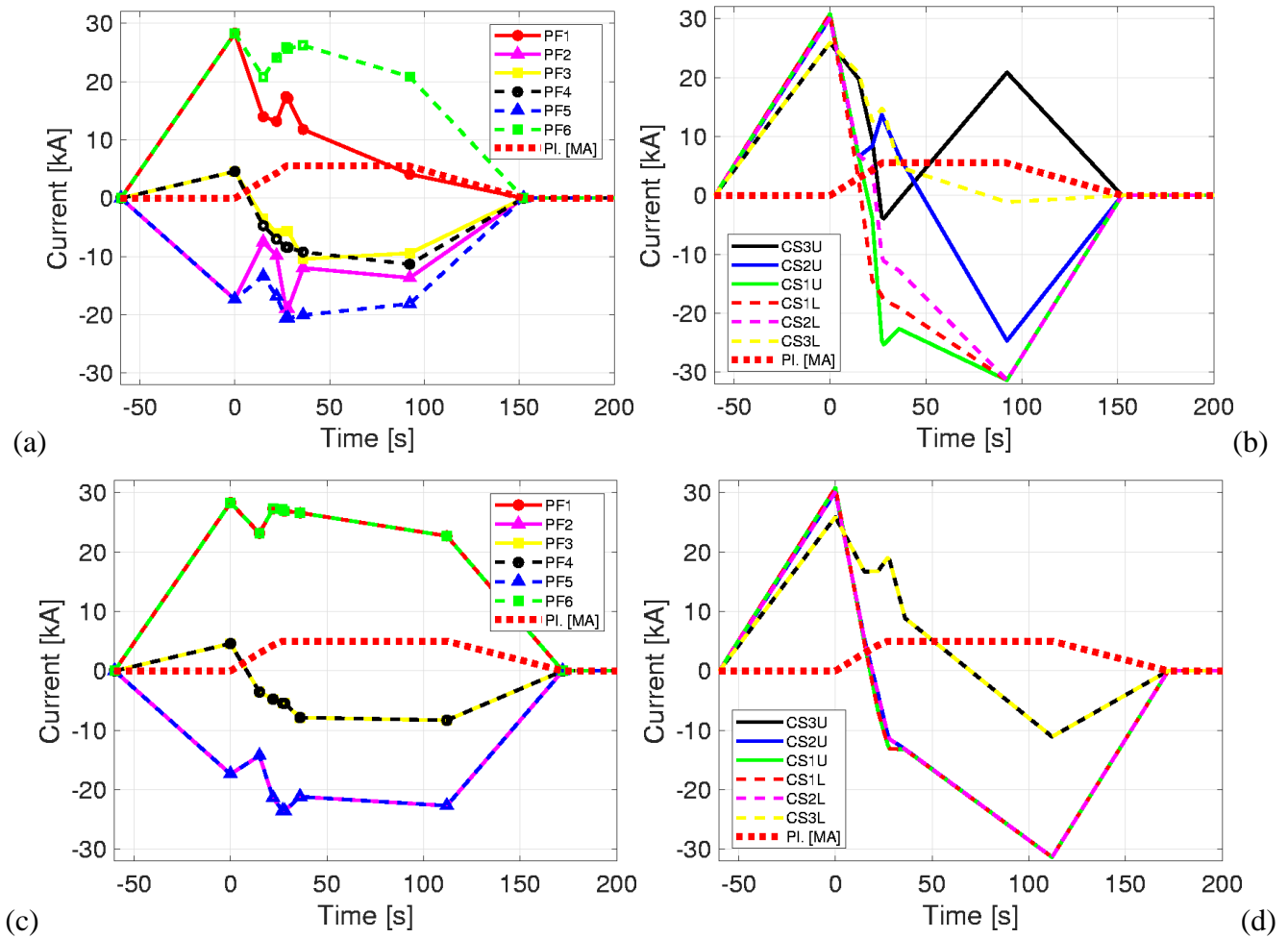
Fig. 3. Current evolution during the SN scenario in all PF coils (a) and in all CS modules (b), and during the DN scenario in all PF coils (c) and in all CS modules (d). The plasma current evolution (Pl.) is also reported in each figure.

2.1 The Poloidal Field coils

Six PF coils are foreseen in DTT, mechanically supported by the outer TF coil structures. In order to improve the flexibility of the machine (letting it explore also perfectly symmetric plasma configurations), the magnet system is symmetric in vertical direction, so PF1 is identical to PF6, PF2 is identical to PF5 and PF3 is identical to PF4. While PF2-5 are wound using NbTi conductors, PF1 and PF6 are made by Nb3Sn in order to withstand the higher magnetic field (up to 9 T) experienced in the region where they are located, quite close to the CS.

Each PF coil is double-pancake (DP) wound, but each pair of identical coils features a different number of DPs and turns/DP: 9 DPs with 20 turns/pancake PF1&6, 8 DPs with 10 turns/pancake PF3&4 and 7 DPs with 14 turns/pancake PF2&5. As sketched in Fig. 4a, in the reference design option ("single-pancake cooling") each pancake is independently cooled: the He inlets, located at the bore of the coil, feed fresh SHe to each DP (similarly to what happens in the ITER CS inlet design [7]), so that the coolant flows turn-by-turn in counter-current in adjacent pancakes, see Fig. 4c. A second design option ("double-pancake cooling"), aiming at reducing the space occupation at the coil bore, implements a DP-cooling

layout. In this case, reported in Fig. 4b, the SHe is fed to each pair of DPs from the outer radius. Thus the coolant splits in one pancake for each of the two adjacent DPs where the inlet is located. After flowing inwards turn-by-turn along that pancake, the coolant reaches the innermost turn. Then it passes in the second pancake of the DP and flows outwards turn-by-turn along it, exiting the coil again at its outer radius. In this case, the He flow will be turn-by-turn in counter-current in adjacent DPs, but will be in co-current in adjacent pancakes of the same DP. This cooling strategy is adopted also in the JT-60SA CS [8]; beside the advantage of concentrating all the hydraulic connections of the coil on its outer radius, it has the drawback of injecting fresh He far from the coil bore, where most of the AC loss power is deposited, reducing the effectiveness of the cooling. This issue will be discussed in the result Section.
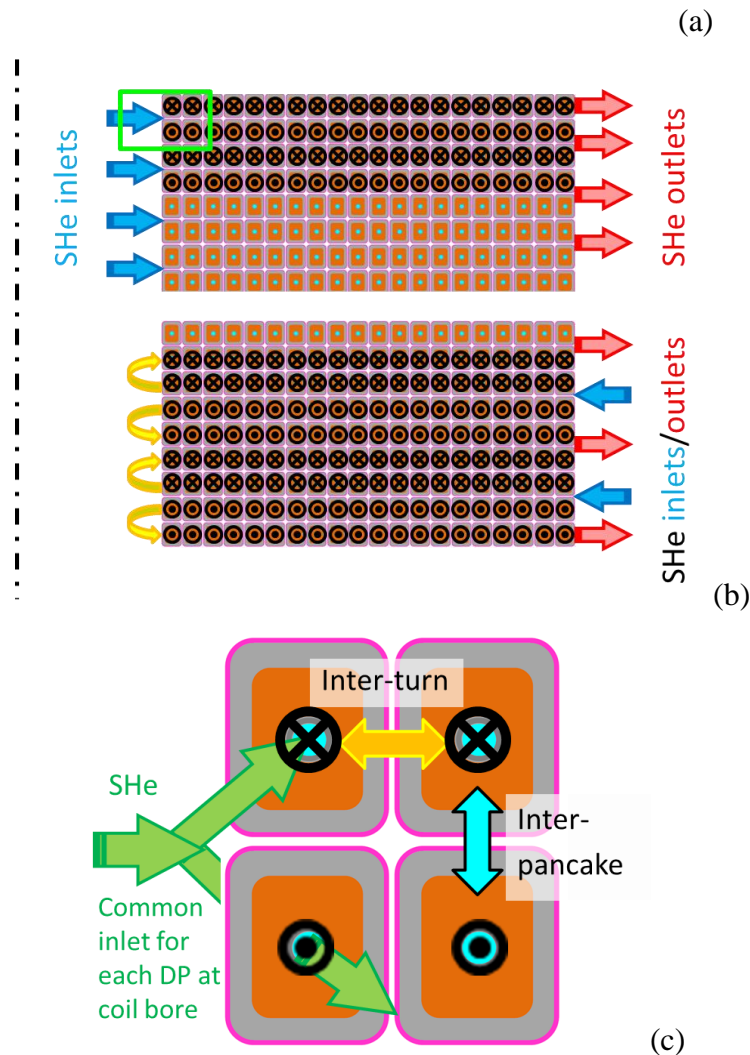

Fig. 4. Radial-vertical cross section of a part of the PF6 coil: the location of the SHe inlets and outlets is indicated both for the single-pancake (a) and the double-pancake (b) cooling options. (c) Zoom on the green rectangle in the top-left part of (a) highlighting the SHe inlet feeding two pancakes and the consequent turn-by-turn counter-current He flow in adjacent pancakes. Inter-turn and inter-pancake heat transfer are also indicated. The black circles with an "×" indicate a flow entering in the page, while those with a dot indicate a flow exiting from the page.

Table 1. Characteristics of the DTT PF conductor.

	PF1&6	PF2&5	PF3&4
Number of SC strands (D_{str} = 0.82mm)	180 (Nb3Sn)	162 (NbTi)	324 (NbTi)
Number of Cu strands (D_{str} = 0.82mm)	216	324	162
Cu:nonCu ratio in strands	1	1.9	1.9
Void fraction (%)	29.8	27.9	27.9
Central channel ID/OD (mm)	5/7	5/7	5/7
Jacket thickness (mm)	3.0	3.0	3.0
CICC vertical side (mm) – non insulated	27	26.5	26.5
CICC horizontal side (mm) – non insulated	20.6	22.9	22.9
Turn insulation thickness (mm)	1.4	1.4	1.4
Hydraulic channel length (m) for single-pancake cooling	180	190	380

In Table 1 the main conductor characteristics are reported. Note that the NbTi conductor geometry is identical for both PF2&5 and PF3&4: the conductor of the two pairs of coils only differ in the number of superconducting (SC) and copper strands. In addition to the 1.4 mm electrical G10 turn-insulation, each DP is wound by a 1 mm insulation layer. In view of the pretty long hydraulic length, ranging from ~180 m to ~380 m, all the CICCs are equipped with a central channel (also called "hole") delimited by a spiral in order to provide a low-impedance pressure relief channel.

2.2 The Central Solenoid

The DTT Central Solenoid (CS) is made by 6 identical modules stacked vertically, as, for example, the ITER CS [9]. Each module is layer-wound, in order to exploit the possibility of grading the jacket and superconductor cross section, optimizing cost and space occupation. Three different conductors are used to build three submodules, called High Field (HF, close to the coil bore), Medium Field (MF) and Low Field (LF), see Fig. 5. The HF and MF submodules are made by four layers (17 turns/layer in the HF, 20 turns/layer in the MF), while the LF is wound with 6 layers with 24 turns each. The three submodules

are connected electrically with 2 intermediate joints. On top of the electrical G10 turn-insulation, an additional 1 mm insulation layer separates two adjacent submodules.
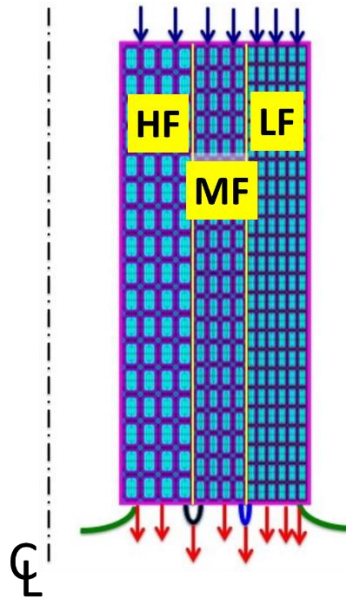

Fig. 5. Radial-vertical cross section of one of the lower CS modules: the location of the SHe inlets (top) and outlets (bottom) is indicated. HF = high field, MF = medium field, LF = low field.

The SHe inlets are located on the base of the modules closer to the machine equator. Similarly to the PF coils, each inlet feeds two adjacent layers, thus each module features 7 inlets and 8 outlets, since the latter are staggered with respect to the former. Also in this case, adjacent layers will experience turn-by-turn counter current He flow.

The most relevant conductor and coil characteristics are reported in Table 2. All the conductors are rectangular without any central pressure-relief channel, because the hydraulic length is quite small with respect to, e.g., the DTT PF coils or the ITER CS conductor hydraulic length.

Table 2. Characteristics of the DTT CS conductor.

	HF	MF	LF
Number of SC strands (D_{str} = 0.82mm)	810	300	180
Number of Cu strands (D_{str} = 0.82mm)	0	159	216
Cu:nonCu ratio in strands	1	1	1
Void fraction (%)	26.5	27	27
Jacket thickness (mm)	4.9	3.9	2.0
CICC vertical side (mm) – non insulated	44.34	37.39	30.83
CICC horizontal side (mm) – non insulated	28.17	20.17	15.51
Turn insulation thickness (mm)	1.0	1.0	1.0
Hydraulic channel length range (m)	47 – 57	70 – 79	98 – 111

The only important difference among the modules that is expected to have an impact on the thermal-hydraulic performance of the CS is the operating current and, in turn, the magnetic field in the conductor. This is due to two reasons: first because, in order to comply with the plasma scenario, either SN or DN, each module carries a different current; second because of the different position in the machine.

3 4C code model

The 4C code [10] is used here to model both the 6 PF coils and the 6 CS modules of DTT and analyze their thermal-hydraulic performance during plasma operation. While the generic features of the 4C code are described in detail in [10], the model characteristics most relevant for the case at hand are reported here.

3.1 Thermal-hydraulic model

Each hydraulic channel (the He cooling path in the CICC constituting the coil, from the He inlet to the He outlet, namely the pancake for the single-pancake cooling option and the DP for the double-pancake cooling option) is described by a set of 1D transient mass, momentum and energy conservation equations computing the SHe velocity, pressure and temperature along the channel in the two regions (the central

channel and the bundle). The heat conduction equation is solved in the two solid regions (namely, the strands and the jacket). In the winding pack (WP), the thermal coupling between adjacent turn and pancakes/layers is also modeled (properly accounting for the co- or counter-current He flow): the inter-turn and inter-pancake (ITIP), or inter-layer (for the CS), insulation is considered as a pure thermal resistance between two neighboring jackets, as described in [11]; an equivalent heat transfer coefficient H_{ITIP} (expressed in $W \cdot m^{-2} \cdot K^{-1}$) can then be defined as:

$$H_{ITIP} = M \cdot k/\delta$$

where k is the insulation thermal conductivity, δ the total insulation thickness and M is a parameter accounting for both the multi-layer nature of the wrapped insulation and the uncertainty on the effective thickness of the insulation and resin (after the impregnation), having different thermo-physical properties. This parameter needs to be calibrated on model coils, but in most of the calibration exercises it is found to be not far from ~0.2 as, e.g., in JT-60SA CS [12] and KSTAR PF coils [13]. This value will thus be taken as the reference one, but a parametric scan between 0 (adiabatic turns and pancakes) and 1 (nominal thermal coupling) will be performed for the DTT PF coils.

Being the relevant details of the cryogenic circuit supplying SHe to the PF coils and the CS still unknown at this design stage, constant thermal-hydraulic boundary conditions are applied to the coil boundaries. In particular, the inlet pressure is set to 6 bar, while the 1 bar design pressure drop is prescribed across each coil (2 bar only in the case of DP cooling, as the hydraulic length of each channel is doubled): the outlet pressure is thus set to 5 bar (4 bar in the case of DP cooling). The inlet temperature is set to 4.5 K. These are design values allowing an optimal operation of the cryoplant, in line, e.g., with the operation of existing superconducting tokamaks as JT-60SA [12] and KSTAR [13]. Prescribing constant boundary conditions may affect the computation of the minimum temperature margin, because in a closed circuit operated with a SHe circulator the strong heat deposition during the plasma initiation phase can induce a backflow at the hydraulic channel inlet, due to the He expansion, especially in the (pancake-wound) PF coils where the maximum power is deposited close to the inlet. However, the lack of information on the circuit and circulator itself does not allow, for the time being, to account for that effect.

The modified Darcy-Forchheimer correlation [14] is used for the calculation of the friction factor in the bundle of both PF coils and CS conductor. The correlation developed for the circular channels with spiral-walls of the ENEA design of the EU DEMO TF conductor [15] is used for the determination of the friction factor in the hole of the PF coils, as the size of the hole in the two conductors is equal.

The heat transfer coefficient between He and solids is computed by means of the Dittus-Boelter correlation [16], as described in [17] and references therein.

3.2   Magnetic field

The magnetic field variation is the main driver of the thermal-hydraulic transient. For this reason, a new strategy is adopted here for its evaluation, allowing to reduce the need for electro-magnetic calculations when changing the scenario to be analyzed.

OPERA tool [18] is used to compute the magnetic field components $B_x(x_i,y_i,z_i,j)$, $B_y(x_i,y_i,z_i,j)$, $B_z(x_i,y_i,z_i,j)$ in the 3 spatial directions x, y, and z induced in each point i (x_i,y_i,z_i) of interest in the space (namely, in each turn of each pancake/layer of each coil) when 1 kA current is carried separately by each other coil, the coil itself and the plasma (generically indicated by j). Then, all these information and the current evolution $I_{op}(t,j)$ in each coil j during the scenario to be analyzed are given in input to the 4C code: it scales the contributions to $B_x(x_i,y_i,z_i,j)$, $B_y(x_i,y_i,z_i,j)$, $B_z(x_i,y_i,z_i,j)$ from each coil (and the plasma) with their operating current $I_{op}(t,j)$, sums all the contribution in each of the 3 spatial directions and computes $|B(x_i,y_i,z_i,t)|$ and $d|B(x_i,y_i,z_i,t)|/dt$.

The magnetic field components need to be computed only once for each geometry, and then all possible current scenarios can be easily modeled only knowing the evolution of the current in each coil and the plasma.

In the calculations reported here, the magnetic field ripple on the PF coils and CS due to the presence of the TF coils is neglected, as well as the magnetic field gradient on the conductor cross section for the CS analyses (while it is considered in the PF analyses, featuring NbTi conductors more sensitive to the magnetic field): the magnetic field on the conductor centerline is used for the calculation of the temperature margin in the CS.

3.3 Critical current parametrization

The "ITER-2008" J_C parametrization from [19] has been adopted here for the Nb_3Sn strands: the critical current is expressed as a function of the magnetic field, strand temperature and axial strain, assumed to be −0.63 % in the PF1 and PF6 coils and CS simulations, constant and uniform along the conductor length. The coefficients reported in Table 3 are used for the above-mentioned scaling.

For the NbTi strands (PF2 to PF5 coils), the critical current parametrization described in [20] is adopted, with the coefficients reported in Table 4. The NbTi critical current depends on the magnetic field and strand temperature only.

Table 3 Coefficients adopted in the parametrization of the scaling law of Nb₃Sn.

Coefficient	Value
C_{a1}	44.48
C_{a2}	0.0
$\varepsilon_{0,a}$ (%)	0.256
ε_m (%)	-0.049
$B_{c2,m}(0)$ (T)	32.97
$T_{c0,m}$ (K)	16.06
C_0 (A×T/mm²)	79220
p	0.63
q	2.10

Table 4 Coefficients adopted in the parametrization of the scaling law of NbTi.

Coefficient	Value
C_0 (A×T/mm²)	1685000
α	1.0
β	1.54
γ	2.1
$B_{c2,m}(0)$ (T)	14.61
$T_{c0,m}$ (K)	9.03

3.4 Driver: the AC losses, nuclear and static heat loads

The AC losses analytical formulae employed in the 4C model are taken from [21] and summarized below. The model in [21], as many others, is based on the single coupling time constant $n\tau$: it is the main parameter governing coupling losses, determining the time scale of the coupling current transients. It depends on the strands/wires twist pitches and on the inter-filament/strand transverse resistivity. Even though multistage cables have multiple time constants (one for each stage of the twisting), here for simplicity the single effective time constant $n\tau$ is considered, as in [20].

The model described in [21] introduces a saturation parameter, relating the speed of the magnetic field variation, the characteristic time constant and the penetration field B_p (see below). Depending on the speed of the magnetic field variation, then, different formulas are proposed to evaluate the coupling and hysteresis losses.

The coupling losses in the unsaturated (P'_{coup}) or saturated ($P'_{coup,sat}$) regime are computed as follows.

$$P'_{coup}(x,t) = \frac{n\tau}{\mu_0} \left(\frac{dB(x,t)}{dt}\right)^2 A_{SC}$$

$$P'_{coup,sat}(x,t) = \frac{4}{3\pi\mu_0} B_p \left[1 - \left(\frac{I(t)}{I_C(x,t)}\right)^2\right] \left|\frac{dB(x,t)}{dt}\right| A_{SC}$$

where $n\tau$, is the single coupling time constant, is characteristic of a given conductor design, μ_0 is the vacuum permeability, I_C is the critical current and A_{SC} is the cross-section of the composite strand. B_p is computed according to:

$$B_p(x,t) = \frac{\mu_0}{\pi} D_{str} J_C(x,t) \frac{1}{1 + Curatio}$$

where D_{str} is the diameter of the composite strand, J_C is the critical current density and *Curatio* is the ratio between the copper and non-copper cross-section of the composite strand.

The hysteresis losses in the unsaturated (P'_{hyst}) or saturated ($P'_{hyst,sat}$) regime are computed as follows.

$$P'_{hyst} = \left\{\frac{2}{3\mu_0} B_p \left[1 - \left(\frac{I(t)}{I_C(x,t)}\right)^2\right] \left|\frac{dB(x,t)}{dt}\right| + \frac{4}{3} B_p \left(\frac{I(t)}{I_C(x,t)}\right)^2 \left|\frac{dB(x,t)}{dt}\right|\right\} A_{SC}$$

where I is the operating current, I_C is the critical current and A_{SC} is the cross-section of the composite strands and B_p is computed using the following equation

$$B_p(x,t) = \frac{\mu_0}{\pi} D_{eff} J_C(x,t)$$

where D_{eff} is the effective diameter, here assumed equal to 15 μm.

$$P'_{hyst,sat} = \frac{8}{3\pi\mu_0} B_p \left(\frac{I(t)}{I_C(x,t)}\right)^2 \left|\frac{dB(x,t)}{dt}\right| A_{SC}$$

where B_p is computed using the following:

$$B_p(x,t) = \frac{\mu_0}{\pi} D_{str} J_C(x,t) \frac{1}{1 + Curatio}$$

Note that the formulae to compute both coupling and hysteresis losses use the cross-section of the composite strands (A_{SC}), i.e., the total cross-section only of the strands with superconductors.

The total (coupling + hysteresis) losses (per unit length) are set equal to $P'_{coup} + P'_{hyst}$ or to $P'_{coup,sat} + P'_{hyst,sat}$ if the latter is lower than the former. This strategy has been adopted in order not to overestimate unrealistically the AC losses. Indeed, the formulae used for the unsaturated regime are valid in case of slowly varying magnetic field ($\beta = \frac{\frac{n\tau}{2}\left|\frac{dB(x,t)}{dt}\right|}{B_p} \ll 1$). In case of fast magnetic field variation ($\beta \gg 1$), the effect of screening currents is not negligible and as the magnetic field variation increases, the screening layer thickness increases until the entire cable reach J_C, thus the formulae to be adopted are different. A

simple approach to avoid a large overestimation of the losses was to consider the smaller between $(P'_{coup} + P'_{hyst})$ and $(P'_{coup,sat} + P'_{hyst,sat})$. The evolution of the total AC loss power in all PF coils for both scenarios is reported in Fig. 6.
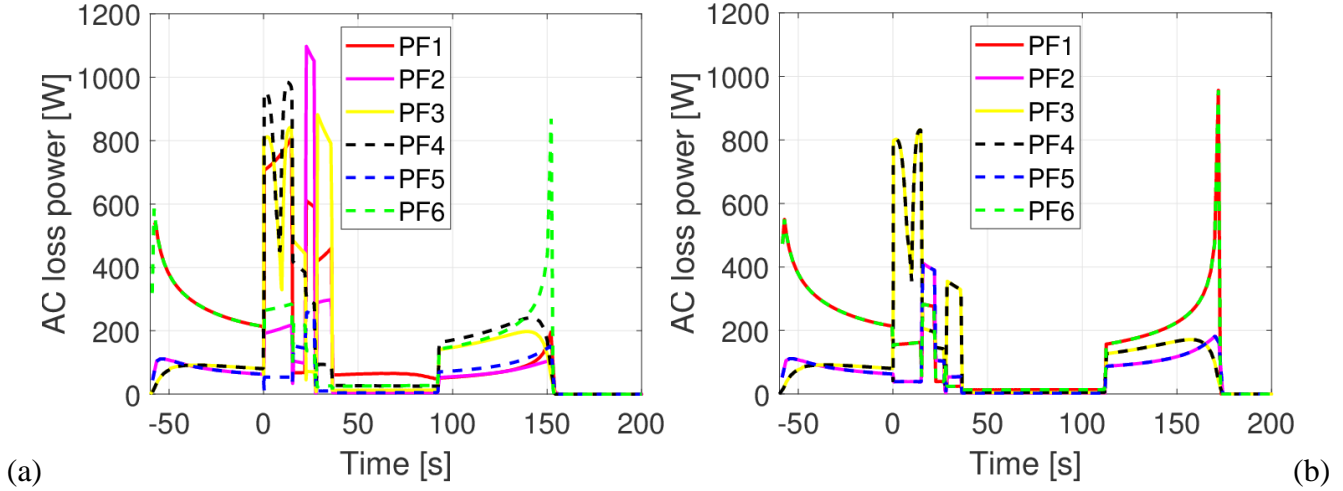

Fig. 6. AC loss power evolution during the SN (a) and DN (b) scenario in all PF coils.

Static (mainly radiative, as the PF are supported by the TF casing which is cooled close to the operating temperature of 4.5 K)) [22] and nuclear [23] heat loads are also considered in the PF coil analysis. The power deposited in each PF coil due to nuclear and static heat load is reported in Fig. 7; the static heat load is deposited during the entire transient uniformly on the coil external surface (it corresponds to a constant heat flux of 1.66 W/m^2), while the nuclear heat load is deposited uniformly in the coil volume and its trapezoidal evolution (according to the plasma pulse) is reported in yellow in Fig. 2. The nuclear heat load is instead not considered in the CS analysis, as it corresponds to ~10 W for each module [23] and is therefore negligible if compared to the AC losses. Moreover, the CS is mechanically supported by the TF structures (cooled to the 4.5 K operating temperature) and its inner and outer surfaces are facing the (cold) CS and TF inner leg, so also the static heat load on the CS is neglected here.

Note that the contribution to the AC losses due to the variation of the plasma current is accounted for, in both CS and PF simulations.
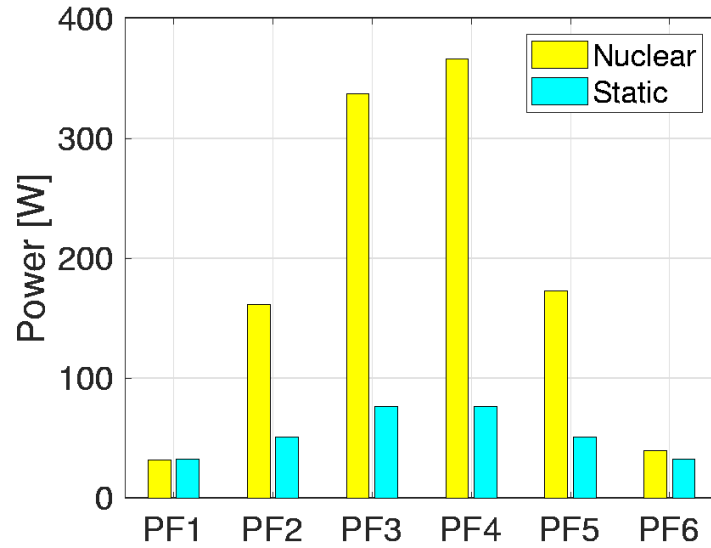
Fig. 7. Distribution of the nuclear and static heat load among the different PF coils, deposited according to the evolution shown in Fig. 2.

4   Results

The results of the thermal-hydraulic analyses are reported in this Section, with reference to the periodic pulse. In the PF coils the H_{ITIP} is varied parametrically, and results for both single-pancake cooling (SPc) and double-pancake cooling (DPc) are compared. The effect of different coupling time constant values is investigated in the CS analysis.

4.1   Poloidal Field coils

4.1.1   Hydraulics

The SHe mass flow rate repartition between bundle and hole within each hydraulic channel is shown in Fig. 8a and compared among the three pairs of PF coils. The total mass flow rate varies from ~ 4 g/s/channel in the PF coils closer to the machine equator (which show the longest hydraulic path) and ~ 6 g/s/channel in PF2&5, with ~ 35-45 % of the He flowing in the bundle. As expected, Fig. 8b shows that doubling the length of the hydraulic path without doubling the pressure head results in a reduction of the mass flow rate of a factor $\sqrt{2}$. For this reason, in the followings the pressure head on each hydraulic channel is doubled in the analysis of the DPc option.
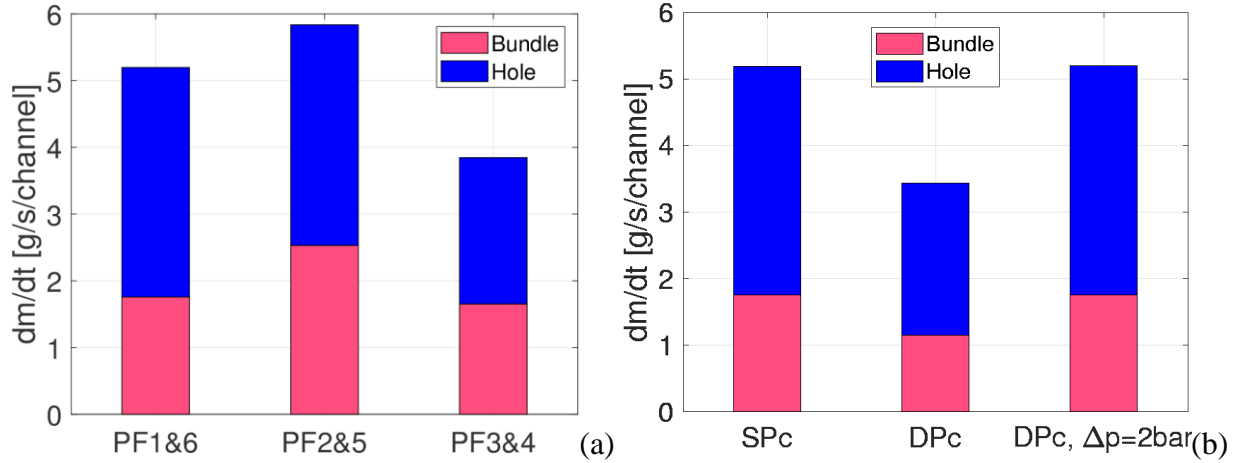
Fig. 8. SHe mass flow rate repartition between bundle (pink) and hole (blue) in (a) each pair of PF coils, for the SPc option, and (b) comparison of the different cooling options, for PF6.

4.1.2 Thermal-hydraulics

The minimum temperature margin ($\Delta T_{\mathrm{marg}}^{\mathrm{min}}$) in each coil for the two scenarios (SPc option) is reported in Fig. 9, assuming $n\tau = 150$ ms for Nb$_3$Sn conductors and 300 ms for NbTi ones. The performance proves to be satisfactory in all coils, as the minimum temperature margin is computed to be everywhere more than 0.2 K above the 1.7 K limit, even considering the static and nuclear heat load (Fig. 9b). Note that the latter, according to Fig. 7, affects more the PF3 and PF4, having a larger radiating surface and being closer to the machine equator.
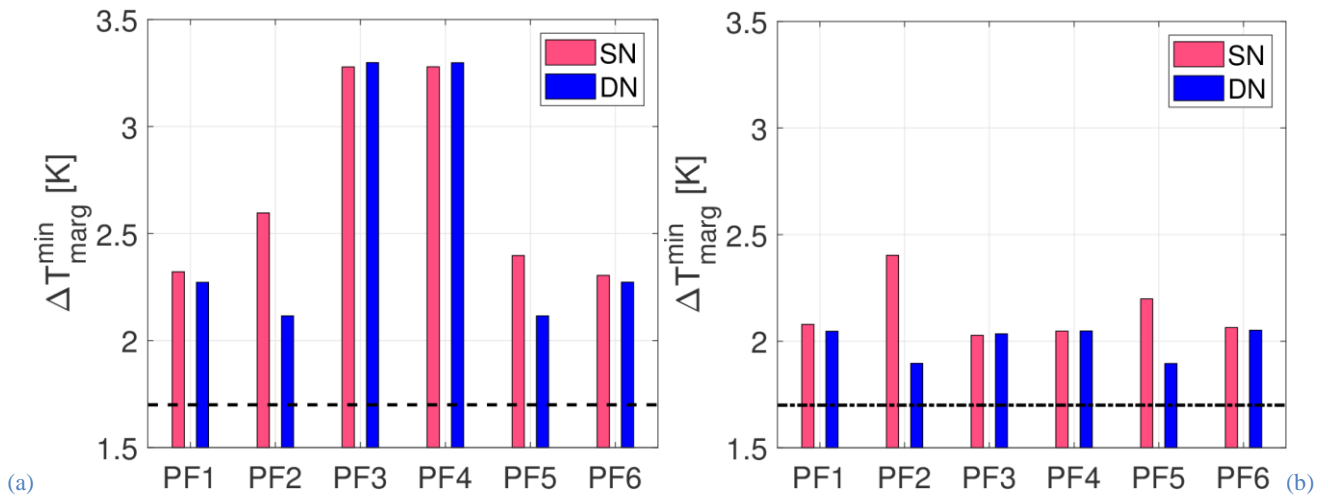

Fig. 9. $\Delta T_{\mathrm{marg}}^{\mathrm{min}}$ in each of the 6 PF coils during SN (pink) and DN (blue) scenarios, for the SPc option, without (a) and with (b) the nuclear and static heat load. The (minimum) acceptance threshold of 1.7 K is also reported (black dashed horizontal line).

Concentrating on PF6 during the SN scenario, the two cooling options have been compared in order to assess their viability. In Fig. 10a, the comparison among the different $\Delta T_{\mathrm{marg}}^{\mathrm{min}}$ is shown also for several

inter-turn and inter-pancake heat transfer coefficient multipliers. The SPc option is almost unaffected by the H_{ITIP}, because the ΔT_{marg}^{min} is localized in the first turn, i.e. close to the cold SHe inlet of all pancakes, so that temperature gradients among the pancakes are small and the heat transfer is negligible: the hot-spot temperature (T_{HS}) is therefore dominated by the heat deposition and not by the ITIP heat transfer. On the contrary, the DPc option suffers two drawbacks. On one hand, the accumulated heat load of the He flowing inwards reduces the ΔT_{marg}^{min} by, e.g., ~ 0.15 K in the adiabatic case with respect to SPc, due to the fact that the He cooling the innermost turns is not as cold as in the SPc option. On the other hand, the effect of the ITIP thermal coupling is stronger: the cold He flowing inwards is pre-heated by the warm He flowing outwards, as already noted and described in detail in the analyses of the JT-60SA CS [12]. As a result, the temperature margin is eroded by additional ~ 0.3 K in the case of nominal thermal coupling ($H_{ITIP}=1$) with respect to the adiabatic case, because of the above-mentioned pre-heating. In reference conditions ($H_{ITIP}=0.2$), the ΔT_{marg}^{min} is eroded by ~ 0.3 K with respect to the SPc option. Even though the cooling of the inner turns is less efficient, the coil performance is still acceptable.

However, the evolution of the T_{HS} and outlet temperature (T_{out}) in PF6 reported in Fig. 10b highlights that the inner turns are not properly (re-)cooled if the DPc option is adopted; the progressive heat accumulation in those turns (experiencing the highest AC losses) during subsequent plasma pulses increases the number of pulses to reach a periodic behavior, and when the latter is reached the minimum T_{HS} is ~ 0.1 K higher than in the case with SPc. Finally, it is possible to appreciate that, while in the SPc case the T_{out} (the only relevant temperature that can be measured in a coil to estimate its temperature margin) is, within few tens of mK, equal to the T_{HS}, this is not the case for the DPc option: the difference in that case is more than 0.3 K, so that it will not be possible to reliably measure the coil temperature margin during operation, without the help of qualified numerical tools, as it was highlighted also in [12].

As a result, and thanks to the space availability to put the SHe inlet at the coil bore, the SPc option is selected for DTT PF coils.
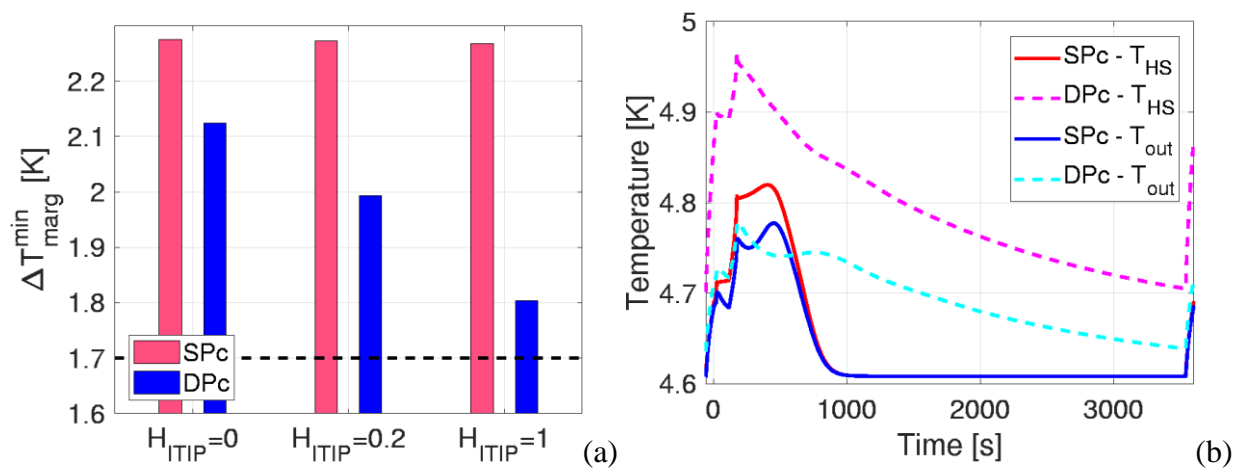

Fig. 10. PF6, SN scenario (without nuclear and static heat load). (a) ΔT_{marg}^{min} in for different cooling options and H_{ITIP} values; the (minimum) acceptance threshold of 1.7 K is also reported (black dashed horizontal line). (b) Evolution of the hot-spot (T_{HS}) and outlet (T_{out}) temperature during the periodic plasma pulse for the two cooling options (the 60 s of the initial PF and CS current

4.2 Central Solenoid

4.2.1 Hydraulics

The DTT CS 4C model takes into account the different He cross-section and the different lengths of each layer. Therefore, since a fixed inlet and outlet pressure is imposed on each layer, a non-uniform mass flow rate is computed for each sub-module and for each layer of each submodule, see Fig. 11. On average, a 5 g/s mass flow rate is obtained in the HF layers, while a mass flow rate equal to ~ 2.5 and ~ 2 g/s flows in the MF and LF layers, respectively. Note that, as the 6 modules are identical in terms of hydraulic design specifications of the conductor, e.g. void fraction and conductor length, the mass flow rate repartition reported in Fig. 11 is expected to be equal in each module. As the layer number increases, they get farther from the coil axis and each turn becomes longer, so that the total length of each hydraulic path increases. This explains the slight decrease of the mass flow rate within each submodule, for increasing layer number. The differences among the submodules are also (and mainly) due to the different geometry of the conductor.
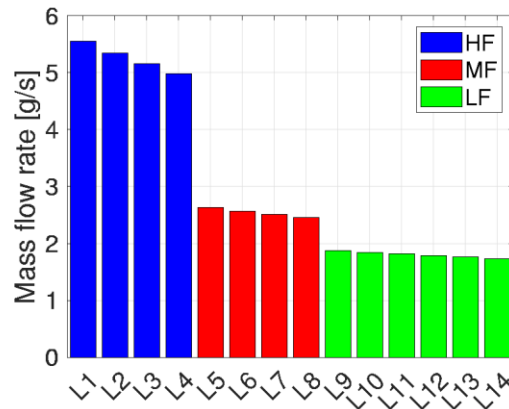

Fig. 11. Mass flow rate in each layer of each submodule of the CS.

4.2.2 Temperature margin

An extensive parametric study on the temperature margin during nominal operation in the DTT CS has been carried out.

Concerning the plasma scenario, in terms of minimum temperature margin, both the SN and DN have been studied for the three different values of $n\tau$ in all the CS modules. Adopting the most conservative value of $n\tau = 300$ ms, for all the modules and in both scenarios, the minimum temperature margin (always located at the first, innermost layer, see below) is larger than the design threshold of 1 K, see Fig. 12a, and the performance are the same for both scenarios, i.e., those modules have almost the same

margin independently on the scenario. This is because both scenarios are characterized by the same maximum value of current (and magnetic field). The difference is that, in the DN scenario, those values are reached at time $t = 112$ s, while in the SN scenario at time $t = 92$ s. This shift in time has a negligible impact on the value of the minimum margin reached in each module.

The parametric study on the $n\tau$ value, which rules the AC (coupling) losses, shows that, as expected, the temperature margin decreases monotonically as $n\tau$ increases, in all modules (see Fig. 12b).

(a)   (b)
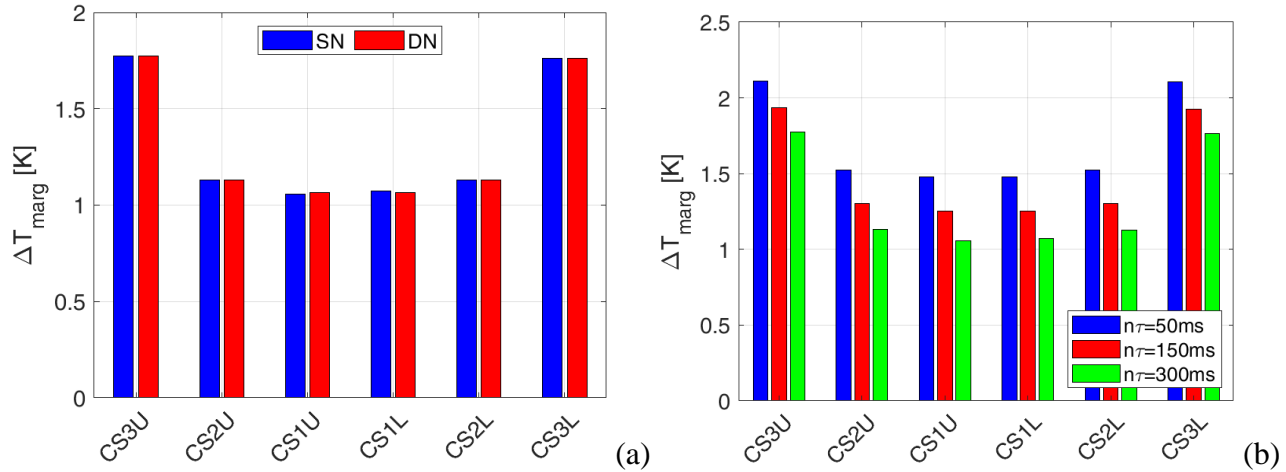
Fig. 12. Comparison of the temperature margin in the first layer of all the modules of the DTT CS varying (a) the plasma scenario (with $n\tau = 300$ ms) and (b) the conductor $n\tau$ in the SN scenario.

The evolution of the temperature margin in the most loaded module (CS1U) in the worst scenario with the largest $n\tau$ value considered (300 ms) is shown in Fig. 13. The comparison among the three submodules shows that the minimum margin is always reached in the first layer, thus in the HF submodule. This result is not straightforward because, even if the MF and LF see a progressively lower magnetic field with respect to HF, they have a different conductor between them and with respect to the HF. In particular, the MF and LF conductors feature a smaller superconductor cross section, and thus are of course less performing than the HF conductor. In view of the higher temperature margin in the MF and, especially, in the LF conductor, some additional optimization of the superconductor grading in the layer designs is maybe still possible.
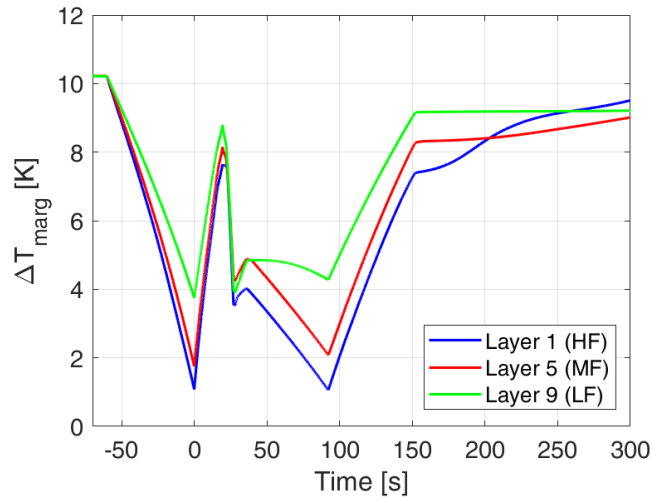
Fig. 13. Evolution of the temperature margin during the first 360 s in the HF, MF and LF submodules of CS1U with $n\tau = 300$ ms (SN scenario).

5   Conclusions and perspective

The DTT PF and CS superconducting coils operated in pulsed mode have been analyzed here with the 4C code to assess their thermal-hydraulic performance in transient plasma pulsed operation.

Within the assumptions and the AC loss model adopted here, all 6 PF coils have proven to withstand the plasma pulsed operation with a minimum temperature margin larger than the design threshold (1.7 K). The options of single- and double-pancake cooling have been compared, showing that the latter, in which the SHe is fed from the outer coil radius, would lead to a 0.3-0.4 K lower temperature margin, and, furthermore, would not allow the estimation of the temperature margin from the outlet temperature reading during operation. In view of the available space in the coil bore, the single-pancake cooling option is then selected.

In the 6 CS modules, the minimum temperature margin is guaranteed to be everywhere larger than the 1 K limit, if the coupling time constant of the conductor is smaller than or equal to 300 ms (according to the assumptions and the modelling adopted). At this stage, this value is then suggested as a reference for the conductor acceptance tests, for both CS and PF coils.

In future, a more detailed check of the breakdown phase will be performed, adding also the SHe cooling circuit and possibly investigating the impact of a wider range of SHe supply temperature and pressure on the temperature margin. Other transients will also be analyzed, with special reference to the off-normal ones, such as quench and effects of a plasma disruption.

Acknowledgements

References

[1] G. Federici, et al., "DEMO design activity in Europe: progress and updates," *Fus. Eng. Des.*, **136**, 729-741 (2018); http://dx.doi.org/10.1016/j.fusengdes.2018.04.001

[2] A.J.H. Donné, G. Federici, X. Litaudon, D.C. McDonald, Scientific and technical challenges on the road towards fusion electricity, J. Instrum. 12 (10) (2017), http://dx.doi.org/10.1088/1748-0221/12/10/C10008 art. no. C10008.

[3] G. Mazzitelli, et al., "Role of Italian DTT in the power exhaust implementation strategy," Fusion engineering and design, 2019, vol.146, p.932-936.

[4] R. Albanese, et al., "Design review for the Italian Divertor Tokamak Test facility," Fusion Engineering and Design 146 (2019) 194–197.

[5] R. Martone, R. Albanese, F. Crisanti, P. Martin, and A. Pizzuto (ed.), "Divertor Tokamak Test facility: Interim Design Report", ISBN: 978-88-8286-378-4, April 2019, "Green Book") https://www.dtt-dms.enea.it/share/s/avvglhVQT2aSkSgV9vuEtw. Accessed on Nov. 30, 2020.

[6] R. Bonifetto, A. Di Zenobio, L. Muzzi, S. Turtu, R. Zanino, and A. Zappatore, "Thermal-hydraulic analysis of the DTT Toroidal Field magnets in DC operation," IEEE Transactions on Applied Superconductivity, vol. 30, issue 4, Jun. 2020, Art. ID 4200605. DOI: 10.1109/TASC.2020.2964517.

[7] R. Zanino, N. Martovetsky, A. Pasquali, L. Savoldi Richard, and D. Speziani, "Computational thermal-hydraulic analysis of the helium inlet options for the ITER Central Solenoid," IEEE Trans. Appl. Supercond., vol. 22, no. 3, Jun. 2012, Art. ID. 4902505.

[8] K.Kizu, H. Murakami, K. Tsuchiya, K. Yoshida, K. Nomoto, Y. Imai, T. Minato, T. Obana, S. Hamaguchi, and K. Takahata, "Development of central solenoid for JT-60SA," IEEE Trans. Appl. Supercond., vol. 23, no. 3, Jun. 2013, Art. no. 4200104.

[9] P. Libeyre, N. Mitchell, D. Bessette, Y. Gribov, C. Jong, and C. Lyraud, "Detailed design of the ITER central solenoid", *Fus. Eng. Des.*, 84(7-11), 2009, pp. 1188-1191.

[10] L. Savoldi Richard, F. Casella, B. Fiori, and R. Zanino, "The 4C code for the cryogenic circuit conductor and coil modeling in ITER," Cryogenics, vol. 50, no. 3, pp. 167–176, 2010.

[11] L. Savoldi and R. Zanino, "M&M:multi-conductorMithrandir code for the simulation of thermal-hydraulic transients in superconducting magnets," Cryogenics, vol. 40, no. 3, pp. 179–189, 2000.

[12] R. Bonifetto, L. Savoldi, and R. Zanino, "Thermal-Hydraulic Analysis of the JT-60SA Central Solenoid Operation," IEEE Transactions on Applied Superconductivity, vol. 29, issue 5, Aug. 2019, Art. ID 4201005.

[13] L. Savoldi Richard, F. Casella, B. Fiori, and R. Zanino, "4C code analysis of thermal-hydraulic transients in the KSTAR PF1 superconducting coil," Cryogenics, vol. 53, Jan. 2013, pp. 37–44.

[14]   M. Lewandowska and M. Bagnasco, "Modified friction factor correlation for CICC's based on a porous media analogy", *Cryogenics*, 51(9), 2011, pp. 541-545.

[15]   R. Bonifetto, P. Bruzzone, V. Corato, L. Muzzi, L. Savoldi, B. Stepanov, R. Zanino, and A. Zappatore, "Thermal–hydraulic test and analysis of the ENEA TF conductor sample for the EU DEMO fusion reactor," IEEE Transactions on Applied Superconductivity, vol. 28, issue 4, Jun. 2018, Art. ID 4205909.

[16]   F. Incropera and D. Dewitt, "Fundamentals of Heat and Mass Transfer," Hoboken, NJ, USA: Wiley, 2006, 6th edition.

[17]   R. Zanino, S. De Palo, and L. Bottura, "A two-fluid code for the thermohydraulic transient analysis of CICC superconducting magnets," Journal of Fusion Energy, vol. 14, 1995, pp. 25-40.

[18]   https://www.3ds.com/products-services/simulia/products/opera/ accessed on Nov. 29, 2020.

[19]   L. Bottura and B. Bordini, "$J_C(B,T,\varepsilon)$ Parametrization for the ITER Nb_3Sn Production", *IEEE Trans. Appl. Supercond.*, 19(3), 2009, pp. 1521-1524.

[20]   L. Bottura, "A Practical Fit for the Critical Surface of NbTi," IEEE Transactions on Applied Superconductivity, vol. 10, no. 1, Mar. 2000, pp. 1054-1057.

[21]   N. Pompeo and L. Muzzi, "The superconducting proposal for the CS magnet system of FAST: a preliminary analysis of the heat load due to AC losses", *arXiv*, 1101.5825, 2011.

[22]   G. Barone, and S. Roccella, "Thermal Shield," presented at DTT Design Review Meeting 03, Frascati, June 19-20, 2019 (https://www.dtt-dms.enea.it/share/page/site/dtt/document-details?nodeRef=workspace://SpacesStore/d26fb83e-e55c-4b14-ad6f-de41413c4bf9).

[23]   R. Villari, B. Caiffi, A. Colangeli, D. Flammini, N. Fonnesu, R. Luis, G. Mariano, and F. Moro, "Nuclear loads for SC magnets design," presented at DTT Design Review Meeting 03, Frascati, June 19-20, 2019 (https://www.dtt-dms.enea.it/share/page/site/dtt/document-details?nodeRef=workspace://SpacesStore/43fb3f2f-8032-44bc-8c89-68840ba1616b).